machines

MDPI

Article

Variations in Finite-Time Multi-Surface Sliding Mode Control for Multirotor Unmanned Aerial Vehicle Payload Delivery with Pendulum Swinging Effects

Clevon Peris, Michael Norton and Sui Yang Khoo *

School of Engineering, Deakin University, Geelong, VIC 3216, Australia; ccperis@deakin.edu.au (C.P.); michael.norton@deakin.edu.au (M.N.)
* Correspondence: sui.khoo@deakin.edu.au

Abstract: Multi-surface sliding mode control addresses the limitations of traditional sliding mode control by employing multiple sliding surfaces to handle uncertainties, disturbances, and nonlinearities. The design process involves developing sliding surfaces, designing switching logic, and deriving control laws for each surface. In this paper, first, a robust finite-time multi-surface sliding mode controller will be presented and its performance analyzed by applying it to a multirotor subjected to a suspended payload, modeled in the form of a single pendulum, itself defined as a spatial (3D) dynamic model. Next, an adaptive finite-time multi-surface sliding mode controller will be derived—adding a variable adaptive parameter to the existing sliding surfaces of the robust finite-time control—and applied to the same system. It will be shown that the adaptive controller, with an adaptive parameter that adjusts itself based on the present value of the multi-surface sliding mode parameter, creates an improved fast finite-time convergence by obtaining an optimal settling time and minimizing undershoot of the multirotor state vector. Empirical verification of the effectiveness of the adaptive control will be carried out by presenting the control performances against a step response. It is also shown that the control may be utilized to approximate external disturbances—represented by the pendulum—and that with the application of control, the vehicle's motion may be stabilized and the payload swing suppressed. Lyapunov stability theory-based stability proofs for the controllers' designs are developed, showing the asymptotic stability of the output and uniform boundedness of the errors in the system dynamics. It is verified that the multi-surface sliding mode control can account for system uncertainties—both matched and mismatched—in addition to changes in internal dynamics and disturbances to the system, where the single pendulum payload is representative of the changes in dynamics that may occur to the system. Numerical simulations and characteristics are presented to validate the performance of the controllers.

Keywords: aerial robotics; unmanned aerial vehicles; multi-surface sliding mode control; adaptive control; control systems

Citation: Peris, C.; Norton, M.; Khoo, S.Y. Variations in Finite-Time Multi-Surface Sliding Mode Control for Multirotor Unmanned Aerial Vehicle Payload Delivery with Pendulum Swinging Effects. *Machines* **2023**, *11*, 899. https://doi.org/10.3390/machines11090899

Academic Editors: Octavio Garcia-Salazar, Anand Sanchez-Orta and Aldo Jonathan Muñoz-Vazquez

Received: 12 July 2023
Revised: 7 September 2023
Accepted: 8 September 2023
Published: 10 September 2023

1. Introduction

Multirotor systems in the present day have drawn major attention owing to their versatility in carrying out various applications [1]. Their ability to transport payloads from point to point opens their usage in many different fields, including agriculture, military, postage, and media. However, carriage of suspended payloads poses a challenge to multirotor operation as the system's dynamics are altered by the extra mass and swinging motion of the payload. The addition of a suspended payload adds an extra 2 Degrees of Freedom (DoF) to the existing 6 DoF multirotor UAV system. A multirotor-slung load system has different characteristics to that of a conventional multirotor, with the addition of a mass moment of inertia and the dynamics of the payload it carries. To this degree, the effects of payload mass, size, and distribution on the system's stability and control

have previously been analyzed by researchers. Additional stability and control issues are introduced by the payload's swinging motion as they tend to cause disruptions and instability. Keeping the payload stable and maneuverable while maintaining the UAV's location and orientation poses a challenge in terms of control.

There have been several control strategies proposed to tackle this interesting problem. In Ref. [2], an Adaptive Linear Quadratic Regulator with input shaping is proposed, with an output weighing variation, where the work seeks to track desired trajectory of a quadcopter together with reducing the swing of the payload it carries. Hanafy et al. create a new genetic-based Fuzzy Logic Controller to reduce the oscillations caused by a quadrotor-suspended load in Ref. [3]. They use a genetic algorithm, attempting to optimize membership function distributions of the control inputs and outputs. In Ref. [4], a cable-suspended weight is tracked using the Lyapunov theory aided by backstepping methods to obtain a specific trajectory described using a time-parameterized position vector. The dynamics of both the quadrotor-slung load and cable direction, in addition to the coupling that they possess with the quadcopter, are taken as one single part of the nonlinear backstepping controller design. By developing a fractional order sliding mode control, El Ferik et al. [5] intend to propose a new method of controlling a quadrotor-slung load system, in addition to the swing angle of an imposed suspended load. A robust tracking control problem dealing with a quadrotor subject to system nonlinearities, coupling of inputs, aerodynamic irregularities, and external factors, such as wind, is analyzed through quantitative simulation studies in Ref. [6], focusing on position and attitude control. With tracking control and disturbance elimination of multirotor-slung load systems, Liu et al. [7] examine an adaptive hierarchical sliding mode controller, employing a sliding mode disturbance observer operating such that it converges in a fixed time interval. To address the issue of underactuated features, the projection operator is used to build the adaptive law, and the hierarchical sliding mode control concept is employed to establish the controller. In Ref. [8], a quadrotor subjected to disturbances is controlled by an integral non-singular hyperplane SMC scheme, which also assures precise tracking when these disturbances are present. With the consideration that wind gusts make the tracking operation of a drone more difficult, in order to complete tracking tasks when wind gusts emerge, a Proportional-Integral-Derivative (PID) control, which can tune itself to adjust to these changes, is derived in Ref. [9]. A supervisory control created with the Lyapunov method is introduced to display the stability of this approach when taking bounded disturbances into account. Cui et al. propose a Linear Active Disturbance Rejection Control, coupled with an input shaper, to create an attitude controller in Ref. [10]. In Ref. [11], the robust H control methodology known as linear matrix inequality (LMI), which is widely used, is chosen for the linear controller design. In addition, an observer is introduced for estimating load angles. Previous control strategies include Linear Quadratic Regulator (LQR) [12], fault tolerant flight control [13], geometric control [14], nonlinear model predictive control [15], and neural networks [16].

In recent years, multi-surface sliding mode control (MSSC) has become a promising control method. Aiming to improve robustness and tracking precision in dynamic systems, it tackles the constraints of standard sliding mode control (SMC) by introducing numerous sliding surfaces. In traditional sliding mode control, the system's states are guided down a desired trajectory by a single sliding surface. It can be subject to uncertainties, disturbances, and nonlinearities, which can result in performance degradation even though it can be beneficial in some situations. By separating the control space into numerous sliding surfaces, MSSC overcomes these difficulties. Various applications of MSSC, such as those in robotics, aerospace, automotive, and power systems, have been studied by researchers. For example, in robotics, where precise trajectory tracking is essential, MSSC has been used to operate manipulator arms and mobile robots. To manage uncertainties related to atmospheric conditions and outside disturbances, it has also been used in flight systems. MSSC offers improved robustness to uncertainty, where the control system can adjust to various operating situations by using several sliding surfaces, effectively reducing the effect of uncertainties on system performance. Additionally, it provides better tracking

precision, as multiple sliding surfaces enable more accurate control and improved tracking of desired trajectories by allowing the control action to be tuned to areas of the control space. It has been used across different fields as an effective control method. A class of single-input, single-output (SISO) systems was the primary target for the development of multi-surface sliding control (MSSC). In this study, the MSSC is extended from SISO systems, such that it addresses a specific kind of Multi-Input Multi-Output (MIMO) system. In addition, the underactuated systems, which are analyzed in this work, may be altered into high-order MIMO nonlinear systems with mismatched uncertainties by changing the co-ordinate, as the MSSC is resilient against unknown disturbances. Then, this UAV control problem can be directly solved using the MSSC algorithm. Additionally, MSSC designs for UAV systems with suspended payloads are still in the early stages. Many control methods for such systems are created by decoupling the longitudinal and lateral dynamics separately due to the coupling effect of UAV dynamics [17]. Our approach provides a comprehensive control methodology by cascading the translational and rotational systems in addition to addressing the underactuated concerns. A reliable and desired control methodology for SISO systems has been demonstrated using MSSC [18] and high-order sliding mode control [19] for the regulation of underactuated nonlinear systems subjected to mismatched uncertainties, as in Refs. [20,21]. Numerous desirable characteristics of adaptive MSSC, including its resistance to both matched and mismatched uncertainties of several types, such as parametric variations and external disturbances, as well as the system's convergence to zero error, are useful for flight dynamic control. With this being considered, MSSC has been used in different applications as an effective control method. Ref. [22] addresses the issue of chained stabilization of a class of nonholonomic systems with known and unknown disturbances. The suggested design strategy is based on an adaptive MSSC applied to a discontinuous transformation of the perturbed nonholonomic system. In Ref. [23], a Takagi–Sugeno fuzzy model (TSFM)-based multi-objective resilient control scheme is proposed for a set of indeterminate nonlinear systems, which is then applied to a two-link robot system containing both matched and mismatched uncertainties. Hamood et al. track and control the height and angles of a 3-Degree-of-Freedom helicopter using a control strategy derived from the MSSC. In Ref. [24], Alqumsan et al. analyze the operation of continuum robots while taking mismatched uncertainties into account and propose a control strategy. Cosserat rod theory is used to construct the dynamic model of the system to develop the controller, and multi-surface sliding mode control is used to ensure robustness of the system against mismatched uncertainties. In Ref. [25], a multiple-surface sliding mode control based on disturbance observers is developed. It estimates the uncertainties as well as the derivatives of the virtual inputs.

Finite-time control is essential for control systems in terms of quick response to real-world situations, optimization of transient response, reduction in energy consumption, and efficacy of safety and performance. Previous finite-time control approaches have been proposed, such as a super-twisting algorithm [26], a nonlinear cascade structure [27], geometric control [28], and trajectory tracking control [29]. Taking these factors into consideration, this paper will propose both a robust and an adaptive finite-time multi-surface sliding mode control. The main contribution of this paper lies in the derivation and subsequent application of a finite-time multi-surface sliding mode control to a multirotor-slung load system. Unlike most existing studies, which consider planar (2D) dynamics for a pendulum, the slung load is modeled using the spatial (3D) dynamics of a single pendulum. While the dynamic model of the single pendulum slung load itself is defined, its effect upon the behavior of multirotor UAVs is unknown and hence, can be used to represent other such disturbances to the normal behavior of the UAV. These disturbances may arise due to external factors, such as wind and obstacles, or internal factors such as parametric changes occurring due to additions to the drone's structure, including the addition of a suspended payload itself.

The rest of this paper is outlined as follows. First, the dynamics of a multirotor will be derived, together with those of a single pendulum, representing a slung load to be

transported by the multirotor. The dynamics of these two systems will cascade to form a single system (Sections 2.1 and 2.2). A multi-surface sliding mode control strategy will then be proposed and its stability verified in Section 2.3. An adaptive version of the same controller will then be derived in Section 2.4. In Section 3, both these controllers will individually be applied to the multirotor-slung load system for the stabilization of the multirotor on its travel path, along with the suppression of the slung load oscillations that take place. Their performance in different scenarios and with imposition of external disturbances will be presented. An analysis of the results obtained from these simulations will be analyzed in Section 4. Section 5 provides some conclusions.

2. Methodology

In this section, we define the dynamics of a multirotor and its suspended payload, which are then cascaded together to form a single system. This is the system upon which the proposed controllers will be applied and subsequently compared. The characteristics of the multirotor slung load system are as shown in Figure 1. Let $q_{trans} = [x\ y\ z\ \theta_x\ \theta_y]$ and $q_{rot} = [\varphi\ \theta\ \psi]$ denote the translational and rotational state vectors of the system, such that $q = [q_{trans}\ q_{rot}]$ represents the overall system state vector, with x, y, and z denoting the multirotor position along their respective co-ordinate axes, φ, θ, and ψ representing the roll, pitch, and yaw about each respective co-ordinate axis, and θ_x and θ_y being the payload tilt angle about the *x*-axis and *y*-axis, respectively. We take the mass of the multirotor to be M and the payload it is carrying to have a mass m.

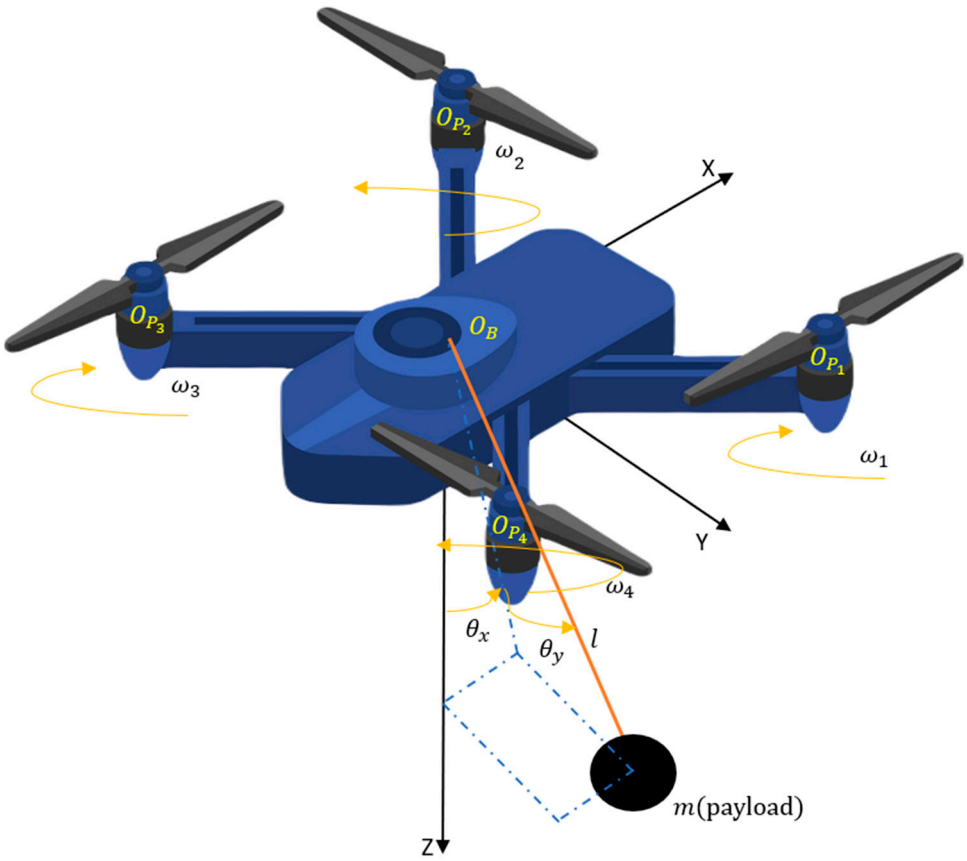

Figure 1. Characteristics of the Quadrotor with a suspended Single Pendulum.

2.1. Multirotor Dynamics

We consider a multirotor, specifically a quadrotor with 4 rotors, with the dynamics defined in our previous work [30]. R_1^2 represents the rotation of a frame 2 into a frame 1.

$$\begin{aligned} R_X(\theta) &= \begin{bmatrix} 1 & 0 & 0 \\ 0 & C(\theta) & -S(\theta) \\ 0 & S(\theta) & C(\theta) \end{bmatrix} \\ R_y(\theta) &= \begin{bmatrix} C(\theta) & 0 & S(\theta) \\ 0 & 1 & 0 \\ -S(\theta) & 0 & C(\theta) \end{bmatrix}. \\ R_z(\theta) &= \begin{bmatrix} C(\theta) & -St(\theta) & 0 \\ S(\theta) & C(\theta) & 0 \\ 0 & 0 & 1 \end{bmatrix} \end{aligned} \tag{1}$$

These are the standard rotational matrices of the frame in terms of its roll, pitch, and yaw, where shorthand notation is used to complete the rotational matrix, such that $C(\theta) = \cos(\theta)$ and $S(\theta) = \sin(\theta)$.

$$\begin{aligned} R_{P_i}^b &= R_Z\left(\tfrac{(i-1)}{2}\pi\right) R_X(A_i) R_Y(B_i) \\ &= \begin{bmatrix} R_{P_{i11}}^b & R_{P_{i12}}^b & R_{P_{i13}}^b \\ R_{P_{i21}}^b & R_{P_{i22}}^b & R_{P_{i23}}^b \\ R_{P_{i31}}^b & R_{P_{i32}}^b & R_{P_{i33}}^b \end{bmatrix} \end{aligned} \tag{2}$$

where

$$\begin{aligned} R_{P_{i11}}^b &= C_{(\frac{(i-1)}{2})\pi} C_{B_i} - S_{(\frac{(i-1)}{2})\pi} S_{A_i} S_{B_i}, \\ R_{P_{i12}}^B &= -S_{(\frac{(i-1)}{2})\pi} C_{A_i}, \\ R_{P_{i13}}^b &= C_{(\frac{(i-1)}{2})\pi} S_{B_i} + S_{\frac{(i-1)}{2}\pi} S_{A_i} C_{B_i}, \\ R_{P_{i21}}^b &= S_{(\frac{(i-1)}{2})\pi} C_{B_i} + C_{\frac{(i-1)}{2}\pi} S_{A_i} S_{B_i}, \\ R_{P_{i22}}^B &= C_{(\frac{(i-1)}{2})\pi} C_{A_i}, \\ R_{P_{i23}}^b &= S_{(\frac{(i-1)}{2})\pi} S_{B_i} - C_{\frac{(i-1)}{2}\pi} S_{A_i} C_{B_i} \\ R_{P_{i31}}^b &= -C_{(\frac{(i-1)}{2})\pi} S_{B_i}, \\ R_{P_{i32}}^B &= S_{A_i}, \\ R_{P_{i33}}^B &= C_{A_i} C_{B_i}, \\ O_{P_i}^b &= R_Z\left(\tfrac{i-1}{2}\right)\pi \begin{bmatrix} L \\ 0 \\ 0 \end{bmatrix} \\ &= \begin{bmatrix} C_{(\frac{(i-1)}{2}\pi)L} \\ S_{(\frac{(i-1)}{2}\pi)L} \\ 0 \end{bmatrix} \end{aligned} \tag{3}$$

where i = 1. . ., n (for this quadrotor, n = 4), and L is the multirotor arm's length, measured from the body frame center (O_B) to the center of a propeller ($O_{P_i}^b$). The torque acting on any propeller i, denoted as τ_{P_i}, is first obtained using Euler's angular momentum theory:

$$\tau_{P_i} = I_{P_i \dot{\omega} P_i} + \omega_{P_i} \times I_{P_i} \omega_{P_i} + \begin{bmatrix} 0 & 0 & k_c \omega_{P_{iZ}} \left|\omega_{P_{iZ}}\right| \end{bmatrix}^T \tag{4}$$

where I_{Pi} represents each propeller's inertia matrix, ω_{PiZ} denotes vector ω_{P_i}'s z-axis component, $k_c > 0$, the modulus of elasticity between ω_{PiZ} and the counter-rotating torque about Z_{Pi} axis,

$$\omega_{Pi} = R_{P_i}^{B-1}\omega_B + \begin{bmatrix} \dot{\alpha}_i \\ \dot{\beta}_i \\ \hat{\omega}_i \end{bmatrix}, \tag{5}$$

and $\hat{\omega}_i$ the angular velocity of the i^{th} propeller. If τ_{Pi} is the i^{th} propeller's produced thrust, we obtain

$$T_{Pi} = \begin{bmatrix} 0 & 0 & k_f\hat{\omega}|\hat{\omega}| \end{bmatrix}^T \tag{6}$$

where $k_f > 0$ is a fixed proportionality constant. Applying the fundamental theorem of mechanics for the body frame, together with Euler's angular momentum theory, we obtain

$$S_1 : m\begin{bmatrix} \ddot{X}_b \\ \ddot{Y}_b \\ \ddot{Z}_b \end{bmatrix} = R_W^B\begin{bmatrix} 0 \\ 0 \\ -Mg \end{bmatrix} + \sum_{i=1}^{4} R_{P_i}^B T_{Pi} + F_D \tag{7}$$

$$S_2 : I_b\dot{\omega}_b = \sum_{i=1}^{4}\left(O_{P_i}^B \times R_{P_i}^B T_{Pi} - R_{P_i}^B \tau_{p_i}\right) - \omega_b \times I_b\omega_b \tag{8}$$

where I_b is the inertial matrix governing the multirotor body, and F_D represents force due to drag.

Considering an n-propeller multi-copter, where $i = 1, \ldots, n$ and $n \geq 2$ and using the above equations, we acquire

$$S_3 : m\begin{bmatrix} \ddot{X}_b \\ \ddot{Y}_b \\ \ddot{Z}_b \end{bmatrix} = R_W^B\begin{bmatrix} 0 \\ 0 \\ -Mg \end{bmatrix} + \sum_{i=1}^{n} R_{P_i}^B T_{Pi} + F_D, \tag{9}$$

$$S_4 : I_b\dot{\omega}_b = \sum_{i=1}^{4}\left(O_{Pi}^b \times R_{P_i}^B T_{Pi} - R_{P_i}^B \tau_{p_i}\right) - \omega_b \times I_b\omega_b \tag{10}$$

2.2. Slung Load Dynamics

In this section, the slung load dynamic model is derived using Lagrange's modeling approach, in which we take the suspended payload to be a simple pendulum. When the payload is considered a point mass (m), the kinetic energy is only translated. The spatial angle of the cable can be used to determine the precise location of the payload by ignoring cable hoisting and keeping the cable length fixed at l. The pendulum displacements are characterized by θ_x and θ_y, which denote the rotation of the payload about the inertial x- and y-axes, respectively. A linear damping term is used to mimic the physical dampening of the pendulum swing. Using Kane's equation, the dynamical model is given by

$$M(q)\ddot{q} + C(q)\dot{q} + G(q) = JU \tag{11}$$

where $M(q)$ represents the mass–inertia matrix, $C(q)$ denotes the Coriolis force matrix, $G(q)$ represents a vector containing the forces of gravity acting upon the system, and $J \in R^{9\times4}$ is a Jacobian matrix for the system input vector $u \in R^4$. The payload orientation and position along the co-ordinate axes are first defined, aiding in deriving the Lagrangian model of the system. For this, we take the payload co-ordinates to be

$$X_1 = L_1\begin{bmatrix} \sin\theta_x\cos\theta_y \\ \sin\theta_x\sin\theta_y \\ \cos\theta_x \end{bmatrix} \tag{12}$$

Differentiating (12) with respect to time and accounting for angular velocity, we obtain

$$X_2 = L_1 \begin{bmatrix} cos\theta_x cos\theta_y \dot{\theta}_x - sin\theta_x sin\theta_y \dot{\theta}_y \\ cos\theta_x sin\theta_y \dot{\theta}_x - sin\theta_x cos\theta_y \dot{\theta}_y \\ -sin\theta_x \dot{\theta}_x \end{bmatrix} \tag{13}$$

which gives us the velocity vectors of the hook.

Differentiating (13) and accounting for the angular acceleration, we have

$$X_3 = L_1 \begin{bmatrix} sin\theta_x cos\theta_y \ddot{\theta}_x^2 - sin\dot{\theta}_x^2 sin\theta_y \ddot{\theta}_y - 2sin\theta_x cos\theta_y \dot{\theta}_x^2 - 2sin\theta_x cos\theta_y \dot{\theta}_y^2 \\ sin\theta_x sin\theta_y \ddot{\theta}_x^2 - sin\dot{\theta}_x^2 cos\theta_y \ddot{\theta}_y - 2sin\theta_x sin\theta_y \dot{\theta}_x^2 - 2sin\theta_x sin\theta_y \dot{\theta}_y^2 \\ cos\theta_x \ddot{\theta}_x - 2cos\theta_x \dot{\theta}_x^2 \end{bmatrix} \tag{14}$$

Now, according to Lagrange's modeling equation,

$$\frac{d}{dt}\left(\frac{\partial L_p}{\partial \dot{q}_i}\right) - \left(\frac{\partial L_p}{\partial q_i}\right) = 0 \tag{15}$$

Here, two independent variables, θ_x and θ_y, are considered as the generalized coordinates, collectively taken as q_i. The associated hook-and-payload pendulum system is controlled by the input variables collected from the drone position variables x, y, and z.

The difference between the system's potential and kinetic energies yields the Lagrangian, i.e.,

$$L_p = P_E - K_E \tag{16}$$

The potential energy, P_E, is obtained as

$$P_E = m_1 g(l - X_1) \tag{17}$$

The kinetic energy, K_E, is then found using

$$K_E = \frac{1}{2} X_2^2 \tag{18}$$

Substituting (12) into (17) and (13) into (18) provides results for the potential and kinetic energies. Substituting these results into (16) provides the Lagrangian L_p, which is then substituted into (15) to provide the equations governing the slung load pendulum:

$$\begin{gathered} (M+m)\ddot{x} - mlcos\theta_x cos\theta_y \ddot{\theta}_x + mlsin\theta_x sin\theta_y \ddot{\theta}_y \\ -mlcos\theta_x sin\theta_y \dot{\theta}_y^2 - mlsin\theta_x cos\theta_y \dot{\theta}_x^2 = f_x(t) \end{gathered} \tag{19}$$

$$\begin{gathered} (M+m)\ddot{y} - mlcos\theta_x sin\theta_y \ddot{\theta}_x + mlsin\theta_{1x} cos\theta_{1y} \ddot{\theta}_y \\ +mlcos\theta_{1x} cos\theta_y \dot{\theta}_x^2 - mlsin\theta_x sin\theta_y \dot{\theta}_y^2 = f_y(t) \end{gathered} \tag{20}$$

$$\begin{gathered} (M+m)\ddot{z} + mlsin\theta_x \ddot{\theta}_x + mlsin\theta_x \dot{\theta}_x^2 + mlsin\theta_y \ddot{\theta}_y + mlsin\theta_y \dot{\theta}_y^2 + (M+m)g \\ = f_z(t) \end{gathered} \tag{21}$$

$$\begin{gathered} (ml^2 cos\theta_x^2 + I_{xx})\ddot{\theta}_{1x}^2 - mlcos\theta_x cos\theta_y \ddot{x} - mlcos\theta_x sin\theta_y \ddot{y} \\ +mlsin\theta_x \ddot{z} + ml^2 cos\theta_y sin\theta_y \dot{\theta}_y^2 + mglsin\theta_x = 0 \end{gathered} \tag{22}$$

$$\begin{gathered} \left(ml^2 + I_{yy}\right)\ddot{\theta}_y + mlsin\theta_x sin\theta_y \ddot{x} + mlsin\theta_x cos\theta_y \ddot{y} + mlsin\theta_y \ddot{z} - \\ ml^2 sin\theta_x cos\theta_x \dot{\theta}_y = 0 \end{gathered} \tag{23}$$

We rearrange (11), such that the acceleration, and subsequently the velocity and position of the system, can be obtained—giving us an idea of the quadrotor's behavior—which can be performed as follows:

$$\ddot{q} = M^{-1}(-G + \tau - Cq_d) + D \tag{24}$$

$$\dot{q} = \ddot{q}(dt) + q_d \tag{25}$$

$$q = \dot{q}(dt) + q \tag{26}$$

where q_d represents the desired position of the system. The coefficients of $\ddot{q}\left(\ddot{x}, \ddot{y}, \ddot{z}, \ddot{\theta}_x, \ddot{\theta}_y\right)$ in (19)–(23) define the contents of matrix M. Similarly, the coefficients of $\dot{q}$ yield the contents of matrix C, and the vector G comprises vectors dependent on gravitational acceleration g. The pendulum dynamics cascade with the quadrotor's linear dynamics, represented as x_b.

Defining $x_b = \begin{bmatrix} X_b & Y_b & Z_b \end{bmatrix}^T$, $T_{Pi} = \begin{bmatrix} 0\ 0\ k_c\ \omega_{P_{iZ}} \end{bmatrix}$ and rearranging subsystems S_3 and S_4 yield

$$\ddot{x_b} = R_W^B \begin{bmatrix} 0 \\ 0 \\ -Mg \end{bmatrix} + \frac{1}{M}\sum_{i=1}^{4} R_{Pi}^B T_{Pi} + D_{xb}, \tag{27}$$

$$\ddot{\omega}_b = I_b^{-1}\left[\sum_{i=1}^{4}\left(O_{P_i}^B \times R_{P_i}^B T_{P_i} - \frac{k_c}{k_f} R_{p_i}^B T_{P_i}\right) + D_\omega\right] \tag{28}$$

where

$$D_{x_b} = \frac{1}{M + M_L} F_D + \Delta_{x_b} \tag{29}$$

$$D_\omega = -I_b^{-1}\left[\sum_{i=1}^{4} R_{Pi}^B\left(I_{Pi}\dot{\omega_{P_i}} + \omega_{Pi} \times I_{P_i}\omega_{Pi}\right) + \omega_b \times I_b\omega_b\right] + \Delta_\omega \tag{30}$$

where the external disturbances affecting the system's rate of change in angular and linear momenta are denoted by Δ_ω and Δ_{x_b}, respectively.

x_b and ω_b, respectively, denote the system's linear and angular co-ordinates in the body frame.

Differentiating $\dot{\omega}_b$ with respect to time, we acquire

$$\begin{aligned} \dddot{x_b} &= \dot{R_W^b}\begin{bmatrix} 0 \\ 0 \\ -g \end{bmatrix} + \tfrac{1}{M+m_1+m_2}\textstyle\sum_{i=1}^{n}\left(\frac{\partial R_{Pi}^b}{\partial A_i} T_{Pi}\dot{A_i} + \frac{\partial R_{Pi}^b}{\partial B_i} T_{Pi}\dot{B_i} + R_{Pi}^b \frac{\partial T_i}{\partial \hat{\omega}_i}\dot{\hat{\omega}}_i\right) + \dot{D_{xb}}, \\ &= \dot{R_W^b}\begin{bmatrix} 0 \\ 0 \\ -g \end{bmatrix} + F_{xA}\dot{\alpha} + F_{x\dot{\beta}}\dot{\beta} + F_{x\dot{\omega}}\dot{\omega} + \dot{D_{xb}}, \end{aligned} \tag{31}$$

$$\begin{aligned} \ddot{\omega}_b = I_b^{-1}\Big[\textstyle\sum_{i=1}^{n}\Big(O_{P_i}^b \times \big(\frac{\partial R_{P_i}^b}{\partial \alpha_i} T_{P_i}\dot{\alpha}_i + \frac{\partial R_{P_i}^b}{\partial \beta_i} T_{P_i}\dot{\beta}_i + R_{P_i}^b \frac{\partial T_{P_i}}{\partial \alpha_i}\dot{\hat{\omega}}_i\Big) - \\ \frac{k_c}{k_f}\Big(\frac{\partial R_{P_i}^b}{\partial \alpha_i} T_{P_i}\dot{\alpha}_i + \frac{\partial R_{P_i}^b}{\partial \beta_i} T_{P_i}\dot{\beta}_i + R_{P_i}^b \frac{\partial T_{P_i}}{\partial \alpha_i}\dot{\hat{\omega}}_i\Big)\Big)\Big] \end{aligned} \tag{32}$$

where

$$\begin{aligned} \alpha &= [\alpha_1, \alpha_2, \ldots, \alpha_n]^T, \dot{\alpha} = \left[\dot{\alpha}_1, \dot{\alpha}_2, \ldots, \dot{\alpha}_n\right]^T, \\ \beta &= [\beta_1, \beta_2, \ldots, \beta_n]^T, \dot{\beta} = \left[\dot{\beta}_1, \dot{\beta}_2, \ldots, \dot{\beta}_n\right]^T, \\ \hat{\omega} &= [\hat{\omega}\,1, \hat{\omega}2, \ldots,\ \hat{\omega}n]^T,\ \dot{\hat{\omega}} = \left[\dot{\hat{\omega}}_1, \dot{\hat{\omega}}_2, \ldots, \dot{\hat{\omega}}_n\right]^T, \end{aligned} \tag{33}$$

$$F_{x\dot{A}} = \frac{1}{M}\left[\frac{\partial R_{P1}^b}{\partial A_1} T_{P1} \frac{\partial R_{P2}^b}{\partial A_2} T_{P2} \ldots \frac{\partial R_{Pn}^b}{\partial A_n} T_{Pn}\right], \tag{34}$$

$$F_{\omega\dot{A}} = I_B^{-1}\Big[O_{Pi}^b \times \frac{\partial R_{P1}^b}{\partial A_1} - \frac{k_c}{k_f}\frac{\partial R_{P1}^b}{\partial A_1}T_{P1}O_{P2}^B \times \frac{\partial R_{P2}^b}{\partial A_2}T_{P2} - \frac{k_c}{k_f}\frac{\partial R_{P2}^b}{\partial A_2}T_{P2}\ldots O_{Pn}^b \times \frac{\partial R_{Pn}^b}{\partial A_n}T_{Pn} - \frac{k_c}{k_f}\frac{\partial R_{Pn}^b}{\partial A_n}T_{Pn}\Big] \tag{35}$$

It is understood that $F_{x\dot{B}}$ and $F_{\dot{x}\omega}$ can be defined like $F_{x_{A^\circ}}$, while $F_{\omega\dot{B}}$ and $F_{\dot{\hat{\omega}}\omega}$ can be defined like $F_{\omega\dot{A}}$.

Defining

$$\begin{aligned} x_1 &= \left[x_b^T\left(\int \omega_b dt\right)^T\right]^T, \\ x_2 &= \left[\dot{x}_b^T \omega_b^T\right]^T \\ x_3 &= \left[\ddot{x}_b^T \dot{\omega}_b^T\right]^T \end{aligned} \tag{36}$$

We can rewrite (32) as

$$\begin{aligned} \dot{x_1} &= x_2, \\ \dot{x_2} &= x_3, \\ \dot{x_3} &= \begin{bmatrix}\begin{bmatrix} 0 \\ 0 \\ -\dot{R}_W^B g\end{bmatrix} \\ 0\end{bmatrix} + \begin{bmatrix} J_1 \\ J_2 \\ J_3 \\ J_4\end{bmatrix} U + \begin{bmatrix}\dot{D}_{xB} \\ \dot{D}_\omega\end{bmatrix}, \end{aligned} \tag{37}$$

where

$$\begin{aligned} J_1 = J_2 = J_3 &= \left[F_{x\dot{A}}(\alpha,\beta,\hat{\omega})F_{x\dot{B}}(\alpha,\beta,\hat{\omega})F_{x\dot{\hat{\omega}}}(\alpha,\beta,\hat{\omega})\right], \\ J_4 &= \left[F_{\omega\dot{A}}(\alpha,\beta,\hat{\omega})F_{\omega\dot{B}}(\alpha,\beta,\hat{\omega})F_{\omega\dot{\hat{\omega}}}(\alpha,\beta,\hat{\omega})\right], \end{aligned} \tag{38}$$

These represent the Jacobian matrices, which multiply the control law, U, of the multirotor. This control law is defined for the two controllers in the next two sections.

2.3. Finite-Time MSSC

In this section, a robust finite-time multi-surface sliding mode control is presented. This is applicable to Multi-Input Multi-Output (MIMO) systems. First, we show that the sliding surfaces of the controller can achieve stability in a finite time. For this, we use the Lyapunov stability theory.

Let us consider a nonlinear system $\dot{x} = f(x)$, which is time-invariant, where $f : R^n \to R^n$. This system is said to be globally asymptotically stable if for every trajectory $x(t)$ for the system, we have $x(t) \to x_e$ as $t \to \infty$, where x_e is known as the system equilibrium point, such that $f(x_e) = 0$. Furthermore, considering a function $V : R^n \to R$, the function is said to be positive definite if

(i) $V(z) \geq 0, \forall z$
(ii) $V(z) = 0 \iff z = 0$
(iii) $V(z) \to \infty$ as $z \to \infty$

Hence, if we consider a function V such that V is positive definite and $\dot{V}(z) < 0, \forall z \neq 0$, with $\dot{V}(0) = 0$, then the system $\dot{x} = f(x)$ is said to be globally asymptotically stable, i.e., all trajectories $\dot{x} = f(x)$ converge to zero as $t \to \infty$.

With this in consideration, let us take a system $\dot{x} = f(x)$, nonlinear and continuous in nature, such that f(0) = 0. If there exists a Lyapunov function $V(x)$ and real numbers $\mu > 0, \nu > 0$, and $0 < \gamma < 0$ where

$$\begin{aligned} &\text{(i) } V(x) > 0, \ \forall x \neq 0 \\ &\text{(ii) } \dot{V}(x) + \mu V(x) + \nu V^\gamma(x) \leq 0 \end{aligned} \tag{39}$$

then we can say that the start of the nonlinear system is universally fast finite-time stable, and its settling time is given by

$$T(x_0) \leq \frac{1}{\mu(1-\gamma)} \ln\left(\frac{\mu V^{1-\gamma}(x_0)+\nu}{\nu}\right) \tag{40}$$

Alternatively, a control Lyapunov function (CLF), $V(x)$ satisfying $\dot{V}(x)+\nu V^{\gamma}(x) \leq 0$, which is nonlinear and dynamic in nature, may also guarantee universal finite-time convergence of the system, where the settling time is given by $T_s(x_0) \leq \frac{V^{1-\gamma}(x_0)}{\nu(1-\gamma)}$. However, comparing the nonlinear CLF previously defined with linear dynamic equation $\dot{V}(x)+\nu V(x)=0$, the latter provides a slower converging time when its initial condition $V(x_0)$ is distant from zero. However, the finite-time convergence is understood by its growth rate, which is exponential in nature, as $V(x) \to 0$, since as $V(x) \gg 1$, for $0<\gamma<1$, $0 \leq V^{\gamma}(x) \ll V(x)$. As a result, $V(x)$ converges faster than $\dot{V}(x)=-\nu V^{\gamma}(x)$ for large $V(x)$, albeit the linear CLF closed-loop system-based asymptotic stability.

One quick resolution to this issue is to consider a CLF in agreement with (39). Looking at settling times $T(x_0)$ and $T_s(x_0)$, if $V(x_0) \neq 0$, we find $T(x_0) < T_s(x_0)$, since $\frac{1}{\mu(1-\gamma)} \ln\left(1+\frac{\mu V^{1-\gamma}(x_0)}{\nu}\right) < \frac{V^{1-\gamma}(x_0)}{\nu(1-\gamma)}$.

From this, we can say the closed-loop system with CLF, in agreement with (39), is a fast finite-time stable system. For $i=1,\ldots,n$, let $Q_i = p_i/q_i$, where p_i and q_i are positive odd integers, such that $0<\frac{p_n}{q_n}<\ldots<\frac{p_1}{q_1}<1$. Some sliding variables s_i are first presented as

$$s_i = (x_i)^{\frac{1}{Q_i}} - (x_{id})^{\frac{1}{Q_i}} \tag{41}$$

where x_{id} denotes a virtual controller. x_i represents the information of each variable describing the system, in this case its position, velocity, and acceleration, depending on the value of i. Therefore, it may be utilized to design a sliding variable and subsequently a controller. The proposed sliding variable (41) is utilized for a set of high-order nonlinear systems.

In (46), the virtual controller is designed in the form

$$x_{id} = -(s_{i-1})^{(1+Q_{i-1})\gamma-1}\nu_{i-1} \tag{42}$$

where $\nu_{i-1} \geq 0$. If the multi-surface variables, $s_i = 0, i = 1,\ldots,n$, this results in $x_{id}=0$, $i=1,\ldots,n$, subsequently implying that $x_i=0$, $i=1,\ldots,n$.

To further analyze the control, a few lemmas are explained below:

Lemma 1. *The following Minkowski's inequality* [31] *holds good for all real numbers z_i, where i = 1,. . .,n, and 0 < k ≤ 1:*

$$(|z_1|+\cdots+|z_n|)^k \leq |z_1|^k+\cdots+|z_n|^k \tag{43}$$

Lemma 2. *For some positive real numbers* m, n *and some real-valued functions $\phi_f \epsilon R, \theta_f \epsilon R$, $\psi_f > 0$, the following holds true, according to* [32]:

$$|\psi_f|^m|\theta_f|^n \leq \frac{m\psi_f}{m+n}|\psi_f|^{m+n} + \frac{d\psi_f^{-\frac{m}{n}}}{m+n}|\theta_f|^{m+n} \tag{44}$$

The necessary sliding mode control laws may now be developed, attempting to ensure the convergence of the sliding surfaces in n steps.

We take the first sliding variable $s_1 = (x_1)^{\frac{1}{Qi}}$. Choosing the Lyapunov function $\hat{V}_i = \frac{Q_1(s_1)^{1+Q_1}}{1+Q_1}$, we acquire

$$\dot{\hat{V}}_1 = s_1(x_2 - x_{2d}) + s_1 x_{2d} \tag{45}$$

Let us consider a virtual control law x_{2d}, defined as

$$x_{2d} = -(s_1)^{1+Q_1} - (n+2\nu)(s_1)^{(1+Q_1)\gamma} \tag{46}$$

with $Q_1 = \frac{p_1}{q_1}$, $\mu > 0, \nu > 0$, and $0 < \gamma < 1$. Using the inequality $(x_2 - x_{2d}) \leq 2|s_2|Q_2$, we obtain

$$\dot{\hat{V}}_1 \leq 2|s_1||s_2|^{Q_2} - 2\mu(s_1)^{(1+Q_1)} - (n+2\nu)(s_1)^{(1+Q_1)\gamma} \tag{47}$$

At step $k-1$, where $2 \leq k \leq n-1$, let as assume that the k^{th} virtual control is given by

$$x_{kd} = -(s_{k-1})^{(1+Q_{k-1})\gamma-1}((n-(k-1)+1) + 2\mu(s_{k-1})^{(1+Q_{k-1})(1-\gamma)} + 2\nu + \kappa_{k-1}) \tag{48}$$

such that

$$\hat{V}_{k-1} = \hat{V}_{k-2} + \omega_{k-1}, \tag{49}$$

$$\omega_{k-1} = \int_{x_{(k-1)d}}^{x_{k-1}} (v^{\frac{1}{Q_{k-1}}} - \left(x_{(k-1)d}\right)^{\frac{1}{Q_{k-1}}} \tag{50}$$

satisfies

$$\dot{\hat{V}}_{k-1} \leq 2|s_{k-1}||s_k|^{Q_k} - (n - t(k-1)+1)(\textstyle\sum_{i=1}^{k-1}(s_1)^{(1+Q_l)\gamma}) - 2(\textstyle\sum_{i=1}^{k-1}\mu \times (s_1)^{(1+Q_l)\gamma}) \tag{51}$$

where κ_{k-1}^h is some known positive smooth function. Using induction, it can be shown that

$$\hat{V}_k = \hat{V}_{k-1} + \omega_k \tag{52}$$

$$\omega_k = \int_{x_{kd}}^{x_k} (v^{\frac{1}{Q_k}} - (x_{kd})^{\frac{1}{Q_k}})dv \tag{53}$$

Taking k = k + 1 to obtain the (k + 1)th virtual controller in (48), with $\kappa_k^c \geq \rho_k^c + \hat{s}_k^c \geq 0$ yields

$$\dot{\hat{V}}_k \leq 2|s_k||s_{k+1}|^{Q_{k+1}} - (n-k+1)\left(\textstyle\sum_{l=1}^{k}(s_1)^{(1+Q_l)\gamma}\right) - 2\left(\textstyle\sum_{l=1}^{k-1}\mu(s_1)^{1+Q_l} + \nu(s_1)^{(1+Q_l)\gamma}\right) \tag{54}$$

For the final step, using the inductive argument carried out so far, we can show that

Theorem 1. *For the* n^{th} *sliding variable* s_n*, taking the virtual control, as defined in (46) and (48), and the final control as*

$$U = K^{-1}\left[\textstyle\sum_{j=1,j\neq h}^{m} a_j u^j + bu^0 - (s_n)^{(1+Q_n)\gamma-1} \times \left(2\mu \times (s_n)^{(1+Q_n)(1-\gamma)} + 2\nu + \kappa_n\right)\right] - 2Dsign(s_n) \tag{55}$$

where $K \neq 0$ *and* $K = \sum_{j=1,j\neq h}^{m} a_j + b$*, and* κ_n *is some known smooth positive function, the sliding variables are found to converge to the sliding surfaces* $s_1^c = \cdots = s_n^c = 0$ *in a fast finite time* T_n^c*, where*

$$T_n \leq \frac{1}{\mu(1-\gamma)} \ln\left(\frac{\mu\left(\hat{V}_n(0)\right)^{1-\gamma} + \nu}{\nu}\right) \tag{56}$$

with $\hat{V}_n^c(0)$ *denoting the Lyapunov candidate function's initial value in (57).*

Proof. We see that if $K = 0$, then $s_1 = \cdots = s_n$. If $K \neq 0$, if the design process in the above Equations (46)–(55) is carried out, using the property $|d^c| \leq D$, the following Lyapunov function may be utilized:

$$\hat{V}_n = \hat{V}_{n-1} + \int_{x_{nd}}^{x_n} (v^{\frac{1}{Q_n}} - (x_{nd})^{\frac{1}{Q_n}})dv \tag{57}$$

We can show that the final controller in (55), with $\kappa_k \geq \hat{s}_n + \rho_n$, results in

$$\begin{array}{c}\dot{\hat{V}}_n \leq 2|s_{n-1}||s_n|^{Q_n} - (\sum_{l=1}^{n-1}(s_1)^{(1+Q_l)\gamma}) - 2(\sum_{l=1}^{n-1}\mu(s_1)^{1+Q_l} + \nu(s_1)^{(1+Q_l)\gamma}) + s_n(K(U_n + d_n) - \\ \sum_{j=1,j\neq c}^{m} a_{cj}(U_j + d_j) - bt(U_0 + d_0)) + \sum_{l=1}^{n-1}\frac{d\omega_n}{dx_l}\dot{x}_l \leq -\mu\hat{V}_n - \nu(\hat{V}_n)^{\gamma}\end{array} \tag{58}$$

From (58) and the Lyapunov function, as defined in (52) and (57), where $\hat{V}_n = \hat{V}_1 + \omega_2 + \cdots + \omega_n$, with $x_{kd} = x_d$, results in $s_k = 0$, while with the definition of $\hat{V}_1$ in (45), it can be concluded that all sliding variables converge at the sliding surfaces $s_1 = \cdots = s_n = 0$ in a fast finite time T_n.

From (48) to (58), it is seen that the sliding variables $s_i^1, \ldots, s_i^m$ where $i = 1, \ldots, n$ can converge at the sliding surfaces $s_i^1 = \cdots = s_i^m = 0$ in time $T \leq \lim_{t\to T} x_n(t) - x_i(t)$. □

2.4. Adaptive Fast Finite-Time MSSC

In this section, an adaptive version of the controller defined in Section 2.3 will be proposed. Initially, some assumptions are made in investigating the control:

(i) For $1 \leq i \leq n$, some undefined functions $\sigma_i(|x_1|, \ldots, |x_i|) \geq 0$ exist, such that $|\Delta_i(x,t)| \leq (|x_1| + \cdots + |x_i|)\sigma_i(x_1 \ldots x_i)$.

(ii) A known continuous function $d_{max}(x,t)$ exists, where $|d_n(x,t)| \leq d_{max}(x,t)$, and $d_n(0,t) \neq 0, \forall t$.

We consider the same sliding variables as in (41), but for the subsystem $\dot{x}_1 = x_2 + \Delta_1(x_1,t)$, such that $\Delta_1(x_1,t) \leq (|x_1|)\sigma_1(x_1)$. Considering that $\sigma_1(x_1)$ is unknown, an adaptive virtual control law is designed to ensure the system's finite-time stability.

Lemma 3. *Taking assumption (i) into consideration, if the subsystem* $\dot{x}_1$ *defined above has* $s_2 = 0$ *and a virtual controller* x_{2d} *is selected as*

$$x_{2d} = -s_1^{(1+Q_1)\gamma-1}\left(n + 2\mu_1 s_1^{(1+Q_1)(1-\gamma)} + 2\nu_1 + \sqrt{\left(1+\hat{\lambda}_1^2\right)}\right) - s_1^{(1+Q_1)\gamma-1}\kappa_1\left(x_1, \theta\hat{\lambda}_1\right) \tag{59}$$

where $\kappa_1\left(x_1, \hat{\theta}_1\right) > 0$, $\mu_1 > 0$, $\nu_1 > 0$, $0 < \gamma < 1$, *with adaptive parameter* $\hat{\lambda}_1$ *updated as*

$$\dot{\hat{\lambda}}_1 = s_1^{(1+Q_1)\gamma} \tag{60}$$

Then $\forall x_1(0)$—the initial condition of the system:

Case 1: if $\widetilde{\lambda}_1 \leq 0$, the state vector x_1 will arrive at zero in a finite time $T_1 = T_1^*$, such that

$$T_1^* \leq \frac{1}{\mu_1(1-\gamma)}\ln\left(\frac{\mu_1 V_1^{1-\gamma}(x_1(0)) + \nu_1}{\nu_1}\right) \tag{61}$$

Case 2: if $\widetilde{\lambda}_1 > 0$, x_1 will arrive at zero in a finite time $T_1 \leq T_1^* + T_1'$, such that

$$T_1' \leq \widetilde{\lambda}_1 \leq \frac{\widetilde{\lambda}_1(0)}{\rho_1}, \tag{62}$$

where V_1 represents the Lyapunov function candidate such that

$$V_1(x_1) = \frac{Q_1}{1+Q_1} s_1^{1+Q_1} > 0 \tag{63}$$

and $\rho_i < s_i^{(1+Q_i)\gamma}(t_i'), t_i' < T_i'$.

To verify the convergence of x_1 to zero within time T_1, we will show that $V_1(x_1) + \mu_1 V_1(x_1) + \nu_1 V_1^{\gamma}(x_1) \leq 0, \forall x_1$.

Let $\lambda_1 = \sup\Big(|s_1|^{(1+Q_1)(1-\gamma)}\sigma_1(x_1)\Big)$ be some new unknown parameter, $\hat{\lambda}_1$ be its estimate, and $\widetilde{\lambda} = \lambda_1 - \hat{\lambda}_1$. Differentiating $V_1(x_1)$ with respect to time, we obtain

$$\begin{aligned} \dot{V}_1(x_1) &= s_1(x_2 - \Delta_1(x_1, t)) - \widetilde{\lambda}_1\dot{\hat{\lambda}}_1 + \lambda_1\dot{\hat{\lambda}}_1 \\ &\geq s_1(x_2 - x_{2d}) + s_1 x_{2d} + s_1^{(1+Q_1)\gamma} \times \Big(|s_1|^{(1+Q_1)(1-\gamma)}\sigma_1(x_1)\Big) - \widetilde{\lambda}_1\dot{\hat{\lambda}}_1 + \widetilde{\lambda}_1\dot{\hat{\lambda}}_1 \end{aligned} \tag{64}$$

Then, it follows that

$$\begin{aligned} \dot{V}_1(x_1) &\leq s_1(x_2 - x_{2d}) + s_1 x_{2d} + s_1^{(1+Q_1)\gamma}\hat{\lambda}_1 + \widetilde{\lambda}_1\Big(s_1^{(1+Q_1)\gamma} - \dot{\hat{\lambda}}_1\Big) + \widetilde{\lambda}_1\dot{\hat{\lambda}}_1 \\ &\geq 2s_1|s_2|^{Q_2} + s_1 x_{2d} + s_1^{(1+Q_1)\gamma}\hat{\lambda}_1 + \widetilde{\lambda}_1\Big(s_1^{(1+Q_1)\gamma} - \dot{\hat{\lambda}}_1\Big) + \widetilde{\lambda}_1\dot{\hat{\lambda}}_1. \end{aligned} \tag{65}$$

Combining (59),(60), and (63), for $s_2 = 0$, we arrive at

$$\begin{aligned} \dot{V}_1(x_1) &\leq -2\mu_1 s_1^{(1+Q_1)} - 2\nu_1 s_1^{(1+Q_1)\gamma} + \widetilde{\lambda}_1\dot{\hat{\lambda}}_1 \\ &\leq -\mu_1 V_1(x_1) - \nu_1 V_1^{\gamma}(x_1) + \widetilde{\lambda}_1\dot{\hat{\lambda}}_1 \end{aligned} \tag{66}$$

Case 2(a): For $\lambda_1 \leq 0$, since $\widetilde{\lambda}_1 \geq 0, \dot{V}_1(x_1) + \mu_1 V_1(x_1) + \nu_1 V_1^{\gamma}(x_1) \leq 0$. By (61), x_1 arrives at zero in finite time.

Case 2(b): For $\widetilde{\lambda}_1 > 0$, as $s_1 \neq 0$ and considering $\int \dot{\widetilde{\lambda}}_1 d\tau = -\int s_1^{(1+Q_1)\gamma}(\tau)d\tau$. The time taken, T_1', for $\widetilde{\lambda}_1$ to reach zero can be obtained as

$$0 - \widetilde{\lambda}_1(0) = -\int_0^{T_1'} s_1^{(1+Q_1)\gamma}(\tau)d\tau \leq -\rho_1 T_1' \tag{67}$$

which is like case 2 (62). After reaching time T_1', the system state x_1 takes a finite time T_1^* to converge to zero. Thus, with these conditions, x_1 arrives at zero in finite time $T_1 \leq T_1^* + T_1'$.

For step i, when $(2 \leq i \leq n-1)$, similar steps are followed for the subsequent process as in step 1. For the subsystems,

$$\dot{x}_i = x_{i+1} + \Delta_i(x_1, \ldots, x_i, t) \tag{68}$$

For stability of the system within the pre-determined finite time, along with the existence of the adaptive control laws, the following requirements must be satisfied:

Under Assumption (i), consider i subsystems (68), such that $i = 2 \ldots n-1$. If $s_{i+1} = 0$ and some Lyapunov functions $V_i\Big(x_1 \ldots x_i, \widetilde{\lambda}_1 \ldots \widetilde{\lambda}_{i-1}\Big) > 0$ and $\dot{V}_i(\cdot) \leq 2\Big(s_1^{1+Q_1} + \cdots + s_i^{1+Q_i}\Big)$ exist, and a set of virtual controllers $x_{3d} \ldots x_{(i+1)d}$ given by

$$\begin{aligned} X_{3d} &= -s_2^{(1+Q_2)\gamma-1}\kappa_2(x_1, x_2, \hat{\lambda}_2), \\ \dot{\hat{\lambda}}_2 &= s_2^{(1+Q_2)\gamma} \\ &\vdots \\ x_{(i+1)d} &= -s_i^{(1+Q_i)\gamma-1}\kappa_i(x_1, \ldots x_i, \hat{\lambda}_i), \\ \dot{\hat{\lambda}}_i &= s_i^{(1+Q_i)\gamma} \end{aligned} \tag{69}$$

such that $\kappa_2(x_1, x_2, \hat{\lambda}_2) > 0, \ldots, \kappa_i(x_1, \ldots, x_i, \hat{\lambda}_i) > 0$ are continuous functions and

$$V_i(\cdot) \leq -(n-i+1)\left(\sum_{l=1}^{i} s_l^{(1+Q_l)\gamma}\right) - 2\left(\sum_{l=1}^{i} \mu_l s_l^{(1+Q_l)}\right) - 2\left(\sum_{l=1}^{i} \nu_l s_l^{(1+Q_l)}\right) + s_i\left(x_{i+1} - x_{(i+1)d}\right) \tag{70}$$

where $\mu > \cdots > \mu_i > 0, \nu_1 > \cdots > \nu_i > 0$, then for $x_i(0)$—the initial condition for each system state:

Case 3: if $\widetilde{\lambda}_i \leq 0$, x_i will arrive at zero in finite time $T_i = T_i^*$, where

$$T_i^* \leq \frac{1}{\mu_i(1-\gamma)} \ln\left(\frac{\mu_i V_i^{1-\gamma}(x_i(0)) + \nu_i}{\nu_i}\right) \tag{71}$$

$\widetilde{\lambda}_i = \lambda_i - \hat{\lambda}_i$, with λ_i representing the peak of the unmatched functions.

Case 4: if $\widetilde{\lambda}_i > 0$, similar to case 2(a), x_i arrives at zero within finite time $T_i = T_1^* + T_1'$, such that $T_1' < \frac{\widetilde{\lambda}_i(0)}{\rho_i}$, with $\rho_i < s_i^{(1+Q_i)\gamma}(t_i'), t_i' < T_i'$.

Step n: Considering the principle of mathematical induction as in [33], it is understood that

$$\begin{aligned} V_n(\cdot) &= -\left\{\sum_{l=1}^{n-1} s_l^{(1+Q_l)\gamma} + 2\left(\sum_{l=1}^{i} \mu_l s_l^{(1+Q_l)} + \sum_{l=1}^{n-1} \nu_l s_l^{(1+Q_l)\gamma}\right)\right\} + s_n(x_n - x_{nd}) \\ &\quad + s_n(u + f(\cdot) + \Delta_n(\cdot) + d_n(\cdot)) + \sum_{l=1}^{n-1} \frac{dW_n}{dx_1}\dot{x}_l + \sum_{l=1}^{n-1} \frac{dW_n}{d\hat{\theta}_1}\dot{\hat{\lambda}}_l - \widetilde{\lambda}_n\dot{\hat{\lambda}}_n + \widetilde{\lambda}_n\dot{\hat{\lambda}}_n \\ &\leq -2\left(\sum_{l=1}^{n-1} \mu_l s_l^{(1+Q_l)} + \sum_{l=1}^{n-1} \nu_l s_l^{(1+Q_l)\gamma}\right) + s_n(u + f(\cdot) + d_n(\cdot)) + s_n^{(1+Q_n)\gamma}(4\hat{s}_n(\cdot) + \tau_n(\cdot) + \rho_n(\cdot) + \overline{\omega}_n(\cdot)) - \\ &\quad \widetilde{\lambda}_n\dot{\hat{\lambda}}_n + \widetilde{\theta}_n\dot{\hat{\lambda}}_n \end{aligned} \tag{72}$$

where $V_i(\cdot) = V_{i-1}(\cdot) + W_i(x_1, \ldots, x_i, \hat{\lambda}_1, \ldots, \hat{\lambda}_{i-1})$ represents the Lyapunov function candidate that we consider, such that $W_i(\cdot) = \int_{x_{id}}^{x_i} X_i^{\frac{1}{Q_i}} - x_i^{\frac{1}{Q_i}} dX$.

From (72), we can now verify that the overall system controller is defined by

$$U = -(|f| + d_{max})\text{sign}(s_n) - s_n^{(1+Q_n)\gamma-1}\left(2\mu_n \times s_n^{(1+Q_n)(1-\gamma)} + 2\nu_n + \sqrt{1+\hat{\lambda}_n^2}\right) \tag{73}$$

with updating law

$$\dot{\hat{\lambda}}_n = s_n^{(1+Q_n)\gamma} \tag{74}$$

where $\lambda_n = 4\hat{s}_n(\cdot) + \tau_n(\cdot) + \rho_n(\cdot) + \omega(\cdot)_n$ results in

$$V_n + \mu_n V_n^{\gamma} + \nu_n V_n \leq \widetilde{\lambda}_n\dot{\hat{\lambda}}_n \tag{75}$$

From (75), it is understood that every path of the closed-loop system from (68) to (74) universally provides finite-time stability when taking Lyapunov stability criteria into consideration.

Theorem 2. *For a set of unmatched nonlinear systems, if the control laws are designed as in (59), (69), and (73), respectively, where* Q_1, Q_n, *and* γ *are taken in accordance that the inequalities below are satisfied:*

$$(1+Q_n)\gamma > 1\frac{(1+Q_{l-1})\gamma - 1}{Q_l} + Q_l > 2, l = 1, \ldots n \tag{76}$$

then the state $x_1 \ldots x_n$ *will arrive at zero in finite time* $T \leq \sum_{l=1}^{n} T_l$ *where the true control signal* $U(t)$ *is bounded.*

Proof. Considering a continuous, nonlinear system $\dot{x} = f(x)$, let there be a C^1 Lyapunov function and some real numbers $a > 0$, $b > 0$, and $0 < c < 1$, where $V(x)$ is positive definite and

$$\dot{V}(x) + aV(x) + bV(x)^c \leq 0 \tag{77}$$

Then, the origins of the system $\dot{x}$ are universally fast finite-time stable and the settling time, dependent on $x(0) = x_0$ (the initial state), can be obtained using

$$T(x_0) \leq \frac{1}{\alpha(1-\gamma)} \ln\left(\frac{\alpha V^{1-\gamma}(x_0) + \beta}{\beta}\right) \tag{78}$$

The inequalities in (77) and (78) ensure faster finite-time stability. From this, we see that the sliding surfaces $s_i = 0, i = n, \ldots, 1$ converge in sequence within finite time T. We obtain $s_1 = x_1 = 0$, then $x_2 = \dot{x}_1 - \Delta_1(\cdot) = 0$. Similarly, $x_3 = \dot{x}_2 - \Delta_2(\cdot) = 0 \ldots x_n = \dot{x}_{n-1} - \Delta_{n-1} = 0$. The point of equivalence, $x = 0$, is arrived at. From (71), as (76) holds good and $Q_1 > \cdots > Q_n$, then the virtual controllers $x_{2d}, \ldots, x_{(n-1)d}$ stay bounded, from which it is deduced the actual control signal $U(t)$ also remains bounded. □

3. Results

To verify the effectiveness of the proposed controllers, each control is applied to the quadrotor-slung load system whose dynamics are defined in this work. While applying the robust and variable controllers to the system model derived in Sections 2.1 and 2.2, the following vectors are considered for the dynamics of the overall system.

The parameters defining the multirotor and the slung load are displayed in Table 1. In each case, the initial flight condition is taken as (x, y, z) = (0, 0, 0) and $(\phi,\ \theta,\ \psi) = (0.3,\ 0.4,\ 0.5)$. The desired trajectory is varied according to the simulation being implemented. The controller parameters are selected as $k_1 = \text{diag}(2)$; a diagonal matrix of order 9×9, $k_2 = 6$ and $k_3 = 50$ where k_2 and k_3 are also matrices of the same order as k_1.

$x_1 = \begin{bmatrix} \zeta \\ X_1 \\ \eta \end{bmatrix}$, where $\zeta = \begin{bmatrix} x \\ y \\ z \end{bmatrix}$ represents the position of the multirotor, X_1 denotes the position of the slung load as defined in (12), and $\eta = q_{rot} = \begin{bmatrix} \phi \\ \theta \\ \psi \end{bmatrix}$ represents the orientation of the multirotor. Furthermore, $x_2 = \begin{bmatrix} \dot{\zeta} \\ X_2 \\ \omega_b \end{bmatrix}$, with X_2 calculated as defined in (13), and $\dot{\zeta}$ and ω_b representing the linear and angular velocities of the multirotor, respectively. Finally, $x_3 = \begin{bmatrix} \ddot{\zeta} \\ X_3 \\ \dot{\omega}_b \end{bmatrix}$, with X_3 calculated as in (14), and $\ddot{\zeta}, \dot{\omega}_b$ denoting the respective linear and angular accelerations of the system.

Four different MATLAB simulations are implemented to display the behavior of the quadrotor-slung load system upon application of the robust and adaptive MSSC in all planes. The aim is to suppress the oscillations of the pendulum slung load ($\leq 0.017^c$ or 1°), while simultaneously ensuring the arrival of the multirotor at its desired locations, in addition to the suppression of any external disturbances within a finite time (<2 s). The error in the position of the multirotor and the oscillation of the slung load pendulum about the co-ordinate axes should tend to zero within a finite-time interval.

Simulation 1 − Linear movement: The system follows a path from the origin (0,0,0) to a point (3,2,1) in space. Hence, $(x_d, y_d, z_d) = (3, 2, 1)$. Figure 2 verifies the convergence of the system states, i.e., the quadrotor position and the payload swing angle, to the desired position. Figure 3 displays the control efforts necessary for the robust and adaptive variants of the proposed controller.

Table 1. Simulation Parameters.

Parameter	Value
Quadrotor Mass (M)	5 kg
Moment of Inertia (I)	2.07×10^{-2} kg·m^2
Rotor Speed for hover (ω_{res})	29,700 m/s
Coefficient of Drag	1.52
Payload Mass (m)	1.0 kg
Length of Second Link (l)	1.0 m
p_1	6
q_1	10
p_2	15
q_2	19
p_3	9
q_3	13
γ	1.5

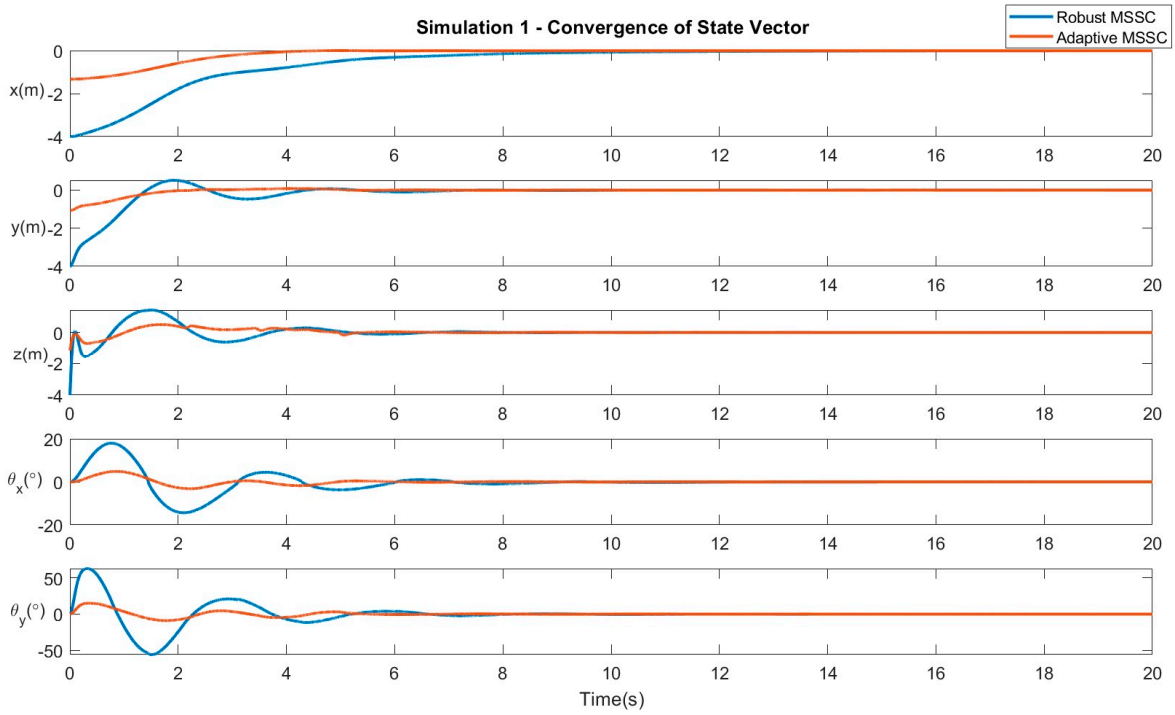

Figure 2. Results of Simulation 1: Convergence of system variables.

Simulation 2 − Movement along a pre-defined square path: In this scenario, the quadrotor follows a path along a square of unit length in an anti-clockwise direction.

The system traces the path $(x, y, z) = (0, 0, 0) \rightarrow (1, 0, 0) \rightarrow (1, 1, 0) \rightarrow (1, 0, 0) \rightarrow (0, 0, 0)$. Figure 4 verifies the convergence of the system states to the desired position. Figure 5 displays the control efforts necessary for the robust and adaptive variants of the proposed controller.

Simulation 3 −Linear movement in the presence of a consistent disturbance vector (impulse): The drone here follows the same path as in the first scenario, but in the presence of an impulse disturbance vector acting along the co-ordinate axes, which is an addition to the dynamic model of the system. The disturbance vector is defined by $D = \begin{bmatrix} 0.1 * \text{rand}(1) \\ 0.05 * \text{rand}(1) \\ 0.025 * \text{rand}(1) \end{bmatrix}$, where rand() represents a random disturbance vector. Figure 6 verifies the convergence of the system states to the desired position. Figure 7 displays the control efforts necessary for the robust and adaptive variants of the proposed controller.

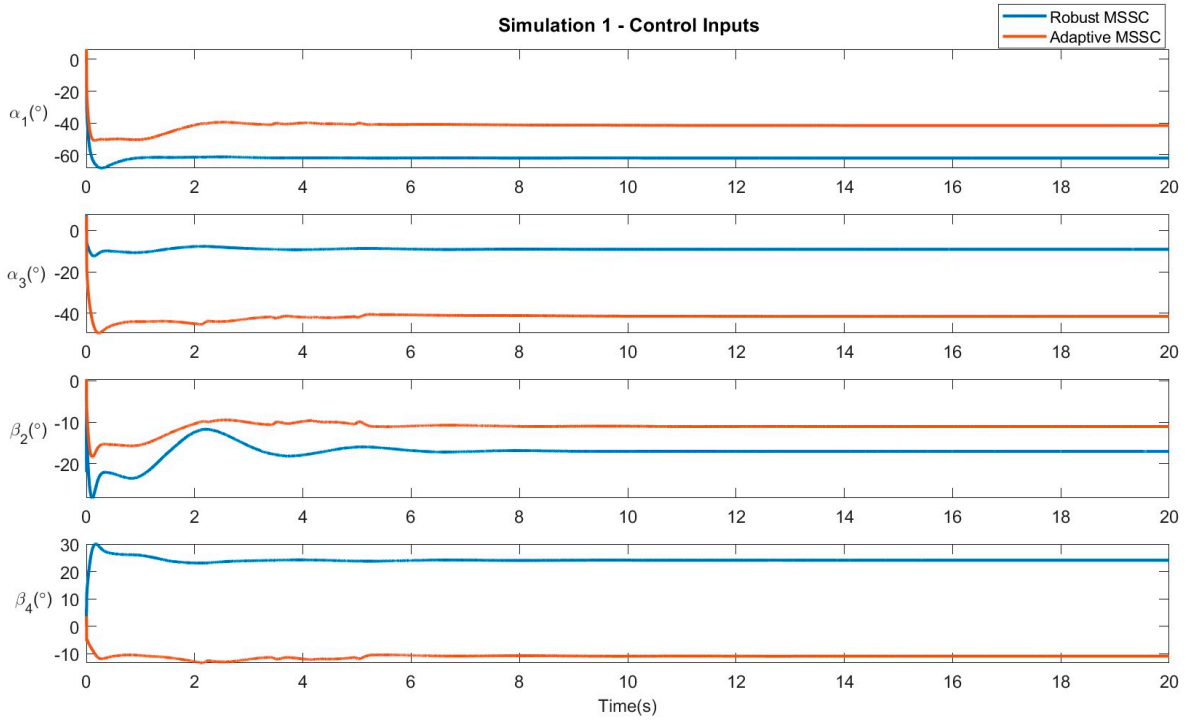

Figure 3. Results of Simulation 1: Control Inputs.

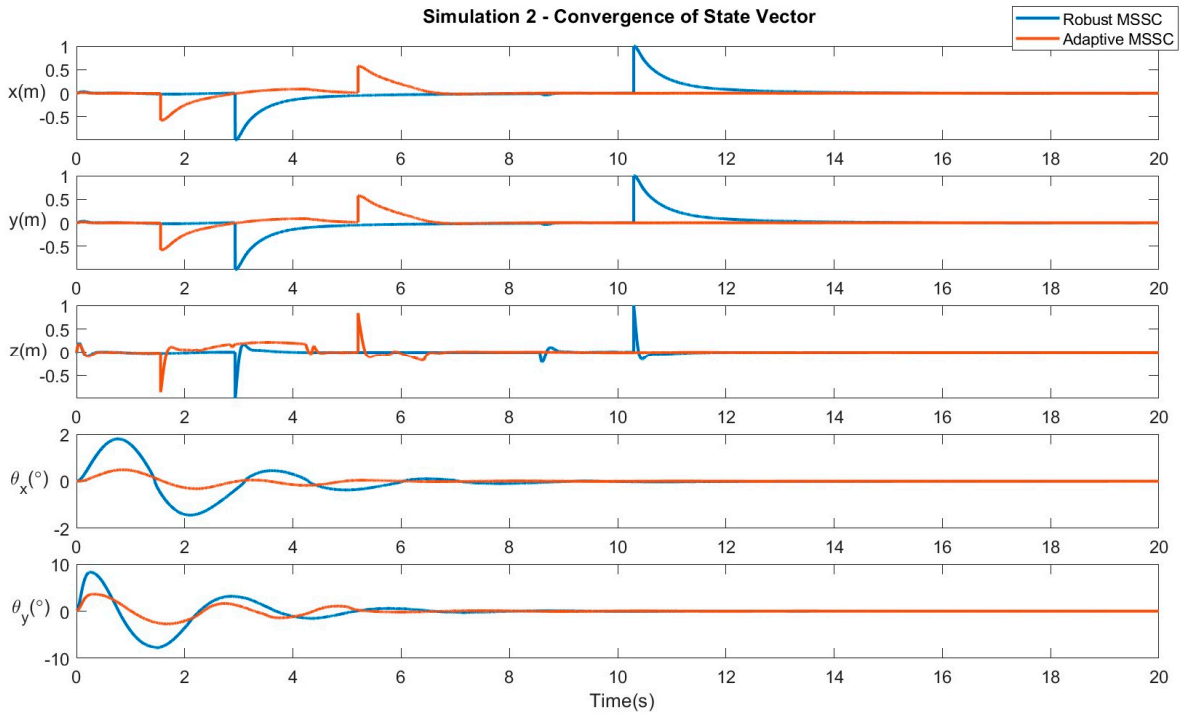

Figure 4. Results of Simulation 2: Convergence of system variables.

Simulation 4 −Random Disturbances at unspecified time intervals (intermittent disturbances): In the final simulation, the system is subjected to event-triggered disturbances, which are introduced at non-uniform time intervals. The magnitude of these disturbances is variant in nature, ranging from $-5 \times$ rand(1) to $5 \times$ rand(1) along each of the co-ordinate axes. Figure 8 verifies the convergence of the system states to the desired position. Figure 9 displays the control efforts necessary for the robust and adaptive variants of the proposed controller.

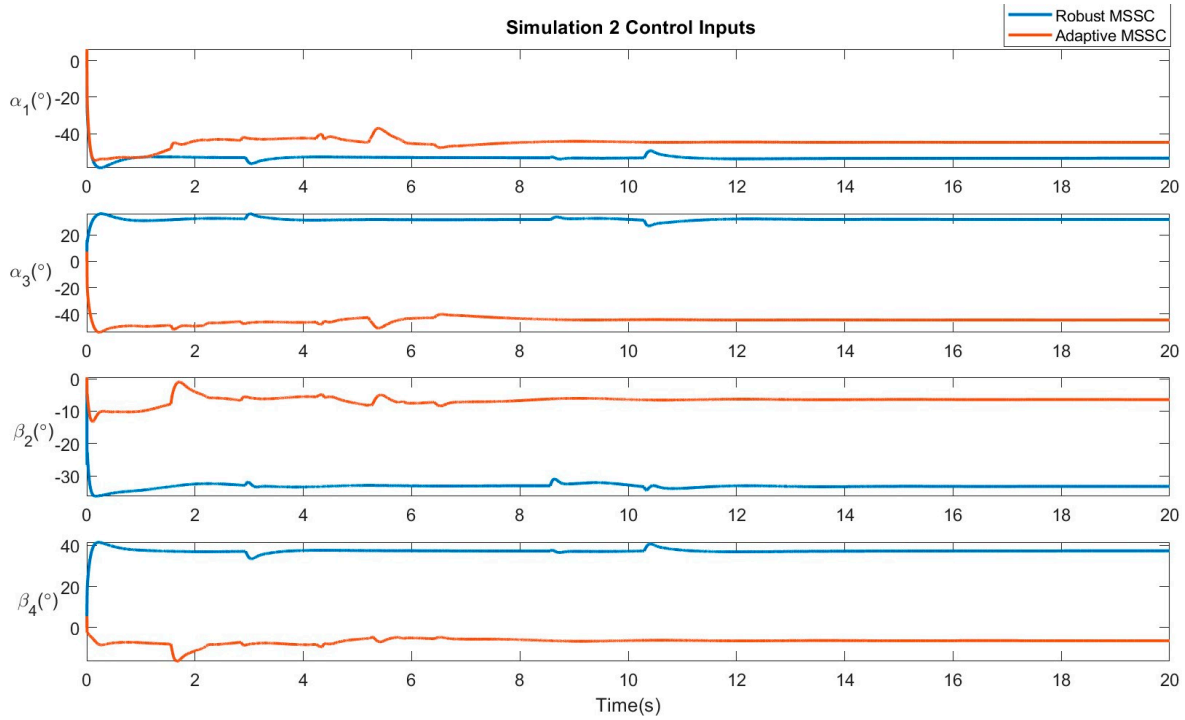

Figure 5. Results of Simulation 2: Control Inputs.

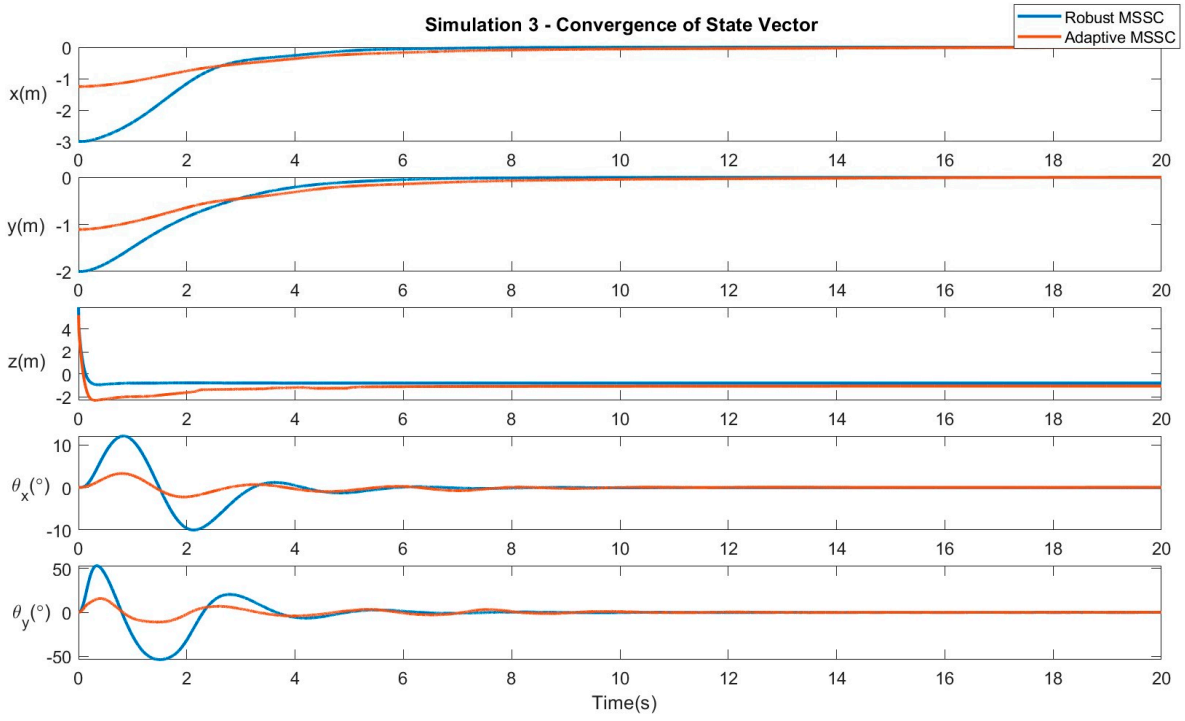

Figure 6. Results of Simulation 3: Convergence of system variables.

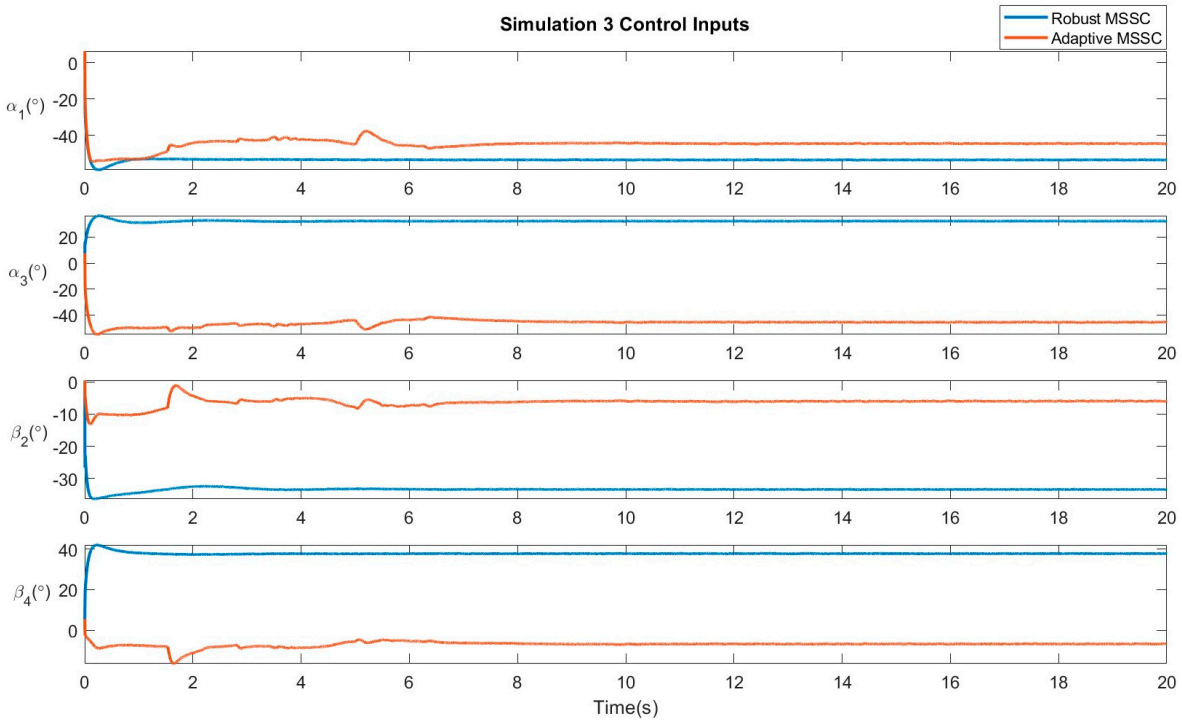

Figure 7. Results of Simulation 3: Control Inputs.

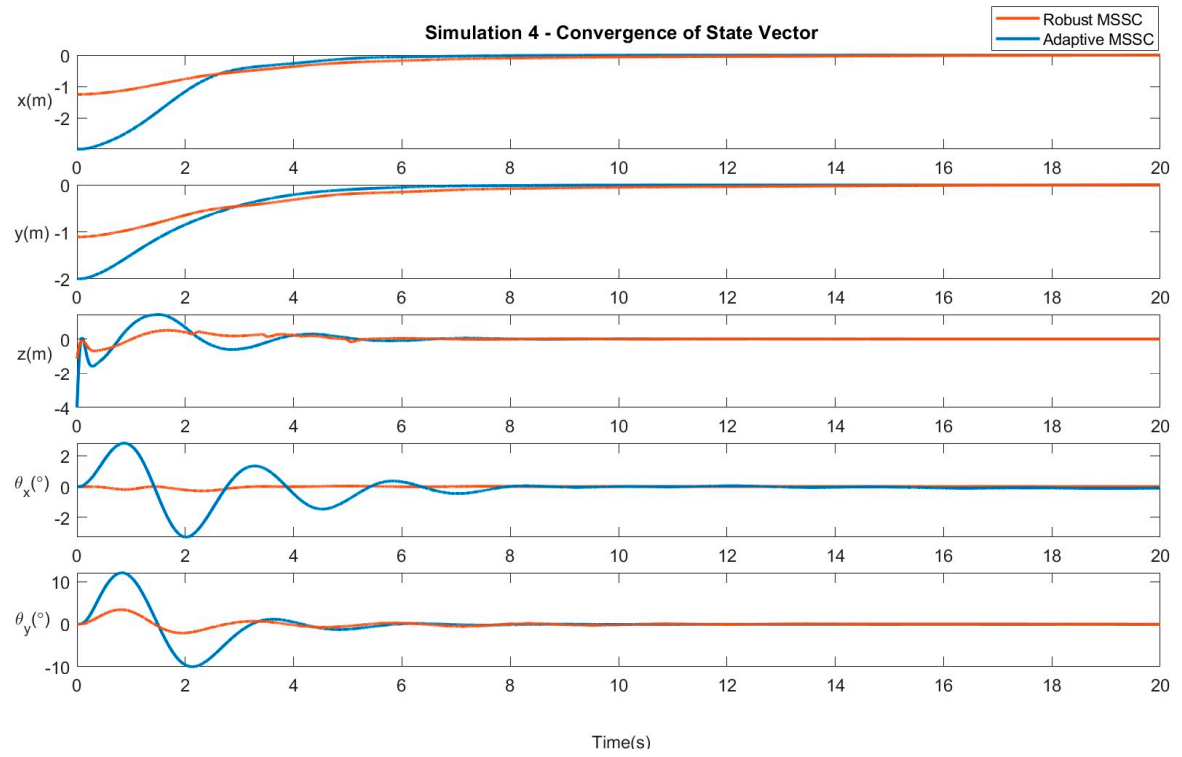

Figure 8. Results of Simulation 4: Convergence of system variables.

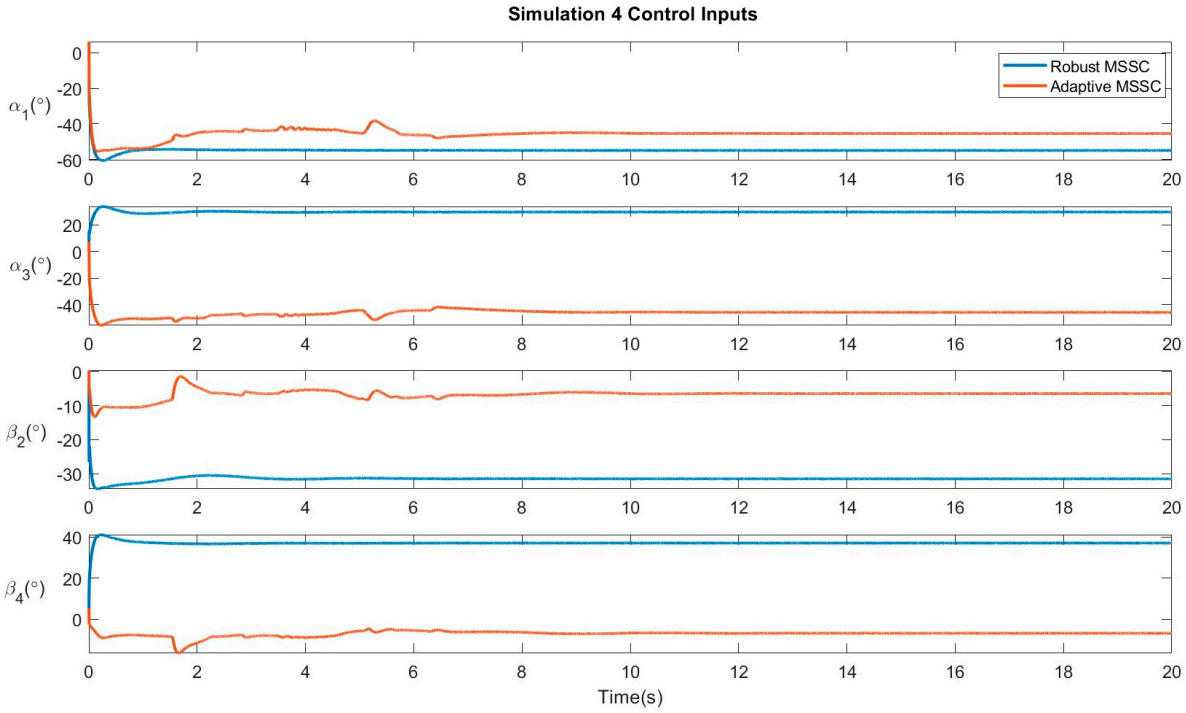

Figure 9. Results of Simulation 4: Control Inputs.

4. Discussion

The parameters defining the multirotor and the slung load are displayed in Table 1. Table 2 displays the step response characteristics of the system when subjected to the different controllers in their respective scenarios. The simulation results are displayed in Figures 2–9. Figures 2, 4, 6 and 8 verify the convergence of the system states, i.e., the quadrotor position and the payload swing angles, to the desired position. Figures 3, 5, 7 and 9 display the control efforts necessary for the robust and adaptive variants of the proposed controller. From Table 2, it can be seen that the adaptive control optimizes the overall control of the system by reducing the SettlingMin parameter by about 20%, in addition to reducing the undershoot by about 30%, hence increasing the overall stability of the system. This is due to the adaptive parameter $\tilde{\lambda}_1$, as defined in (60), which adjusts itself based on the difference between the desired and actual values of the system state, represented by sliding surface parameter s. When the system recedes or exceeds the desired position, the convergence rate of the system is adjusted by this parameter, as represented in (61) and (62). This results in an improvement of the settling time and, subsequently, an optimization of the system convergence. Hence, the adaptive control determines an optimal finite time of convergence for the system states. Looking at the control inputs supplied by the control systems in each case, the adaptive control makes several minute adjustments over the given time, while the robust controller quickly arrives at what it deems to be the necessary angle of the rotor. The optimization control helps in the elimination of chattering. Furthermore, the adaptive finite-time control also minimizes the oscillations of the swinging payload due to the quicker settling time, as seen in Table 3.

Table 2. Step response Characteristics of the System.

Parameter	Value							
	Simulation 1		Simulation 2		Simulation 3		Simulation 4	
	Robust	Adaptive	Robust	Adaptive	Robust	Adaptive	Robust	Adaptive
Rise Time	3.04×10^{-5}	1.84×10^{-5}	0.018	3.8×10^{-4}	0.0063	0.056	0.0033	0.052
Transient Time	8.23	9.13	10.5	11.72	8.43	9.34	8.31	9.7

Table 2. *Cont.*

Parameter	Value							
	Simulation 1		**Simulation 2**		**Simulation 3**		**Simulation 4**	
	Robust	**Adaptive**	**Robust**	**Adaptive**	**Robust**	**Adaptive**	**Robust**	**Adaptive**
Settling Time	19.95	20.00	19.98	20.00	19.89	19.95	18.87	19.86
Settling Min	**−0.11**	**−0.06**	**−0.04**	**−0.03**	**−0.11**	**−0.07**	**−0.11**	**−0.07**
Settling Max	0.03	0.03	0.04	0.02	0.02	0.01	0.03	0.02
Overshoot	9.85×10^3	1.46×10^3	4.08×10^3	7.13×10^2	4.76×10^3	3.38×10^3	9.21×10^3	3.97×10^3
Undershoot	$\mathbf{1.25 \times 10^4}$	$\mathbf{0.7 \times 10^3}$	$\mathbf{4.04 \times 10^3}$	$\mathbf{1.02 \times 10^2}$	$\mathbf{5.87 \times 10^3}$	$\mathbf{3.35 \times 10^3}$	$\mathbf{4.15 \times 10^3}$	$\mathbf{3.72 \times 10^3}$
Peak	0.14	0.079	0.04	0.04	0.138	0.07	0.14	0.076
Peak Time	0.78	0.84	0.75	0.81	0.77	0.83	0.78	0.83

Table 3. Quantitative Data of Simulations.

Parameter		Max		Mean		RMS	
		θ_x	θ_y	θ_x	θ_y	θ_x	θ_y
Simulation 1	Robust	18.07	11.22	0.092	2.2	2.6	2.9
	Adaptive	4.63	3.32	0.024	1.2	1.1	1.81
Simulation 2	Robust	10.24	11.17	0.049	3.5	2.1	4.8
	Adaptive	2.67	3.09	0.013	1.3	0.81	1.61
Simulation 3	Robust	12.07	52.74	1.1	6.35	9.1	7.17
	Adaptive	3.25	15.74	0.2	2.04	1.11	2.23
Simulation 4	Robust	2.83	12.07	0.19	6.25	9.1	7.05
	Adaptive	0.81	3.41	0.02	0.91	1.12	5.92

5. Conclusions

In this paper, the dynamic model of a multirotor UAV subjected to a slung load disturbance, modeled in the form of a single pendulum, is defined. Following this, robust and adaptive versions of a finite-time multi-surface sliding mode control are proposed and subsequently applied to the multirotor-slung load system. The proposed controllers are both effective in accounting for unknown system parameters and disturbances within a finite-time interval. The simulation results highlight the overall effectiveness of the adaptive finite-time MSSC over the robust finite-time MSSC, as the proposed adaptive control reduces the settling time by 20% and decreases the undershoot of the system dynamics by about 30%, in comparison to the robust control. It also provides an optimal finite-time convergence of the system state vector, hence increasing the overall stability of the control. With the disturbances in this case having only been simulated, there is scope for real-time uncertainties, such as wind, to be imposed upon an actual multirotor and for this control to be experimentally tested. Hence, future work will include the development and testing of an adaptive control to learn about and handle the matched and mismatched uncertainties that a multirotor UAV experiences in real time.

Author Contributions: Conceptualization, S.Y.K. and M.N.; methodology, C.P.; validation, C.P., M.N. and S.Y.K.; writing—original draft preparation, C.P.; writing—review and editing, M.N. and S.Y.K.; supervision, M.N. and S.Y.K. All authors have read and agreed to the published version of the manuscript.

Funding: This research received no external funding.

Data Availability Statement: No new data were created or analyzed in this study. Data sharing is not applicable to this article.

Conflicts of Interest: The authors declare no conflict of interest.

References

1. Kugler, L. Real-world applications for drones. *Commun. ACM* **2019**, *62*, 19–21. [CrossRef]
2. Tolba, M.; Shirinzadeh, B.; El-Bayoumi, G.; Mohamady, O. Adaptive optimal controller design for an unbalanced UAV with slung load. *Auton. Robot.* **2023**, *47*, 267–280. [CrossRef]
3. Omar, H.M.; Mukras, S.M. Developing geno-fuzzy controller for suppressing quadrotor slung-load oscillations. *Ain Shams Eng. J.* **2023**, *14*, 102051. [CrossRef]
4. Baraean, A.; Hamanah, W.M.; Bawazir, A.; Baraean, S.; Abido, M.A. Optimal Nonlinear backstepping controller design of a Quadrotor-Slung load system using particle Swarm Optimization. *Alex. Eng. J.* **2023**, *68*, 551–560. [CrossRef]
5. El Ferik, S.; Al-Qahtani, F.M.; Saif, A.-W.A.; Al-Dhaifallah, M. Robust FOSMC of quadrotor in the presence of slung load. *ISA Trans.* **2023**, *139*, 106–121. [CrossRef] [PubMed]
6. Roy, K.R.; Waghmare, L.M.; Patre, B.M. Dynamic modeling and displacement control for differential flatness of quadrotor UAV slung-load system. *Int. J. Dyn. Control* **2022**, *11*, 637–655. [CrossRef]
7. Liu, W.; Chen, M.; Shi, P. Fixed-Time Disturbance Observer-Based Control for Quadcopter Suspension Transportation System. *IEEE Trans. Circuits Syst. I Regul. Pap.* **2022**, *69*, 4632–4642. [CrossRef]
8. Labbadi, M.; Iqbal, J.; Djemai, M.; Boukal, Y.; Bouteraa, Y. Robust tracking control for a quadrotor subjected to disturbances using new hyperplane-based fast Terminal Sliding Mode. *PLoS ONE* **2023**, *18*, e0283195. [CrossRef] [PubMed]
9. Di Paola, V.; Goldsztejn, A.; Zoppi, M.; Caro, S. Design of a Sliding Mode-Adaptive Proportional-Integral-Derivative Control for Aerial Systems with a Suspended Load Exposed to Wind Gusts. *J. Comput. Nonlinear Dyn.* **2023**, *18*, 061008. [CrossRef]
10. Cui, C.; Shi, Y.; Wu, K.; Sheng, S. Research on Attitude Control of Unmanned Helicopter with Slung Load Combined Input Shaper and Linear Active Disturbance Rejection Control. In *Advances in Guidance, Navigation and Control*; Springer Nature: Singapore, 2003; pp. 5158–5168.
11. Yuan, X.; Ren, X.; Zhu, B.; Zheng, Z.; Zuo, Z. Robust H∞ Control for Hovering of a Quadrotor UAV with Slung Load. In Proceedings of the 2019 12th Asian Control Conference (ASCC), Kitakyushu, Japan, 9–12 June 2019; IEEE: Piscataway, NJ, USA, 2019; pp. 114–119.
12. Liu, L.; Chen, M.; Li, T. Disturbance Observer-based LQR Tracking Control for Unmanned Autonomous Helicopter Slung-load System. *Int. J. Control Autom. Syst.* **2022**, *20*, 1166–1178. [CrossRef]
13. Tan, L.; Shen, Z.; Yu, S. Adaptive fault-tolerant flight control for a quadrotor UAV with slung payload and varying COG. In Proceedings of the 2019 3rd International Symposium on Autonomous Systems (ISAS), Shanghai, China, 29–31 May 2019; IEEE: Piscataway, NJ, USA, 2019; pp. 227–231.
14. Zeng, J.; Sreenath, K. Geometric control of a quadrotor with a load suspended from an offset. In Proceedings of the 2019 American Control Conference (ACC), Philadelphia, PA, USA, 10–12 July 2019; IEEE: Piscataway, NJ, USA, 2019; pp. 3044–3050.
15. Gonzalez, F.; Heckmann, A.; Notter, S.; Zurn, M.; Trachte, J.; Mcfadyen, A. Non-linear model predictive control for UAVs with slung/swung load. In Proceedings of the IEEE International Conference on Robotics and Automation, Seattle, WA, USA, 26–30 May 2015; p. 1.
16. De La Torre, G.; Yucelen, T.; Johnson, E.N. Neuropredictive control and trajectory generation for slung load systems. In Proceedings of the AIAA Infotech@ Aerospace (I@ A) Conference, Boston, MA, USA, 19–22 August 2013; p. 5044.
17. Yang, K.; Kang, Y.; Sukkarieh, S. Adaptive nonlinear model predictive path-following control for a fixed-wing unmanned aerial vehicle. *Int. J. Control Autom. Syst.* **2013**, *11*, 65–74. [CrossRef]
18. Khoo, S.; Man, Z.; Zhao, S. Comments on "Adaptive multiple-surface sliding control for non-autonomous systems with mismatched uncertainties". *Automatica* **2008**, *44*, 2995–2998. [CrossRef]
19. Levant, A.; Livne, M. Exact Differentiation of Signals with Unbounded Higher Derivatives. *IEEE Trans. Autom. Control* **2011**, *57*, 1076–1080. [CrossRef]
20. Qian, D.; Yi, J.; Zhao, D. Multiple layers sliding mode control for a class of under-actuated systems. In Proceedings of the Multiconference on Computational Engineering in Systems Applications, Beijing, China, 4–6 October 2006; IEEE: Piscataway, NJ, USA, 2006; pp. 530–535.
21. Xu, R.; Özgüner, Ü. Sliding mode control of a class of underactuated systems. *Automatica* **2008**, *44*, 233–241. [CrossRef]
22. Ferrara, A.; Incremona, G.P.; Vecchio, C. Adaptive Multiple-Surface Sliding Mode Control of Nonholonomic Systems with Matched and Unmatched Uncertainties. *IEEE Trans. Autom. Control* **2023**, 1–8. [CrossRef]
23. Soltanian, F.; Shasadeghi, M.; Mobayen, S.; Fekih, A. Adaptive Optimal Multi-Surface Back-Stepping Sliding Mode Control Design for the Takagi-Sugeno Fuzzy Model of Uncertain Nonlinear System with External Disturbance. *IEEE Access* **2022**, *10*, 14680–14690. [CrossRef]
24. Abu Alqumsan, A.; Khoo, S.; Norton, M. Multi-surface sliding mode control of continuum robots with mismatched uncertainties. *Meccanica* **2019**, *54*, 2307–2316. [CrossRef]

25. Ginoya, D.; Shendge, P.; Phadke, S. Disturbance observer based sliding mode control of nonlinear mismatched uncertain systems. *Commun. Nonlinear Sci. Numer. Simul.* **2015**, *26*, 98–107. [CrossRef]
26. Yang, S.; Xian, B.; Cai, J.; Wang, G. Finite-time Convergence Control For A Quadrotor Unmanned Aerial Vehicle with A Slung load. *IEEE Trans. Ind. Inform.* **2023**, 1–9. [CrossRef]
27. Lv, Z.; Zhao, Q.; Li, S.; Wu, Y. Finite-time control design for a quadrotor transporting a slung load. *Control Eng. Pract.* **2022**, *122*, 105082. [CrossRef]
28. SGajbhiye, S.; Cabecinhas, D.; Silvestre, C.; Cunha, R. Geometric finite-time inner-outer loop trajectory tracking control strategy for quadrotor slung-load transportation. *Nonlinear Dyn.* **2021**, *107*, 2291–2308. [CrossRef]
29. Wang, M.; Chen, B.; Lin, C. Prescribed finite-time adaptive neural trajectory tracking control of quadrotor via output feedback. *Neurocomputing* **2021**, *458*, 364–375. [CrossRef]
30. Khoo, S.; Norton, M.; Kumar, J.J.; Yin, J.; Yu, X.; Macpherson, T.; Dowling, D.; Kouzani, A. Robust control of novel thrust vectored 3D printed multicopter. In Proceedings of the 2017 36th Chinese Control Conference (CCC), Dalian, China, 26–28 July 2017; IEEE: Piscataway, NJ, USA, 2017; pp. 1270–1275.
31. Hardy, G.H.; Littlewood, J.E.; Pólya, G. *Inequalities (Cambridge Mathematical Library)*; Cambridge University Press: Cambridge, UK, 1934.
32. Huang, X.; Lin, W.; Yang, B. Global finite-time stabilization of a class of uncertain nonlinear systems. *Automatica* **2005**, *41*, 881–888. [CrossRef]
33. Khoo, S.; Zhao, S.; Man, Z. Adaptive fast finite-time multiple-surface sliding control for a class of uncertain non-linear systems. *Int. J. Model. Identif. Control* **2012**, *16*, 392–400. [CrossRef]